RSC Advances

ROYAL SOCIETY OF CHEMISTRY

www.rsc.org/advances

Electronic structure and thermoelectric properties of Zintl compounds A_3AlSb_3 (A = Ca and Sr): First-principles study

Qingfeng Shi, Zhenzhen Feng, Yuli Yan, and Yuan Xu Wang*

Institute for Computational Materials Science,

School of Physics and Electronics, Henan University,

Kaifeng 475004, People's Republic of China

(Dated: July 18, 2015)

Abstract

Experimentally synthesized Zn-doped Sr_3AlSb_3 exhibited a smaller carrier concentration than Zn-doped Ca_3AlSb_3, which induces a lower thermoelectric figure of merit (ZT) than Zn-doped Ca_3AlSb_3. We used first-principles methods and the semiclassical Boltzmann theory to study the reason for this differing thermoelectric behavior and explored the optimal carrier concentration for high ZT values via p-type and n-type doping. The covalent $AlSb_4$ tetrahedral arrangement exhibited an important effect on the electronic structure and thermoelectric properties. p-type Ca_3AlSb_3 may exhibit good thermoelectric properties along its covalent $AlSb_4$ chain due to its double band degeneracy at the valence band edge and small effective mass along its one-dimensional chain direction. Zn doping the Al site exhibited higher formation energy for Sr_3AlSb_3 than Ca_3AlSb_3, which explains the lower carrier concentration for Zn-doped Sr_3AlSb_3 than Zn-doped Ca_3AlSb_3. The double band degeneracy at the valence band edge for Ca_3AlSb_3 may also help to increase the carrier concentration. Sr_3AlSb_3 containing isolated Al_2Sb_6 dimers can exhibit a high thermoelectric performance via heavy p-type doping with a carrier concentration above 1×10^{20} holes per cm^3. Moreover, the ZT maxima for the n-type Sr_3AlSb_3 can reach 0.76 with a carrier concentration of 4.5×10^{20} electrons per cm^3.

Keywords: A_3AlSb_3 (A = Ca, Sr), Electronic structure, Thermoelectric performance, Zintl compounds.

* E-mail: wangyx@henu.edu.cn

I. INTRODUCTION

Thermoelectric materials can convert energy between heat and electricity and have attracted significant attention. The conversion efficiency for thermoelectric materials is defined by the dimensionless figure of merit, $ZT = S^2\sigma T/\kappa$, where S, σ, T, and κ are the Seebeck coefficient, electrical conductivity, absolute temperature, and thermal conductivity, respectively. Therefore, a promising thermoelectric material should have a large Seebeck coefficient, high electrical conductivity, and low thermal conductivity. However, S, σ, and κ are always coupled, which makes it difficult for a material to simultaneously have high S, high σ, and low κ. The concept of a "phonon glass electron crystal" (PGEC) is a good approach for achieving good thermoelectric performance. Materials with complex structures often have low intrinsic lattice thermal conductivities and may have good thermoelectric properties [3, 4]. Zintl compounds have emerged as a promising class of materials for thermoelectric applications due to their complex crystal structures[5, 6] and low intrinsic lattice thermal conductivity. For example, the lattice thermal conductivities of Ca_3AlSb_3, Sr_3AlSb_3, and Sr_3GaSb_3 are below 0.6 W/mK at 1000 K[4, 7, 8].

Finding cheap, nontoxic thermoelectric materials with high conversion efficiencies is important. [9] Ca_3AlSb_3 and Sr_3AlSb_3 are promising compounds for thermoelectric applications due to their earth abundant, nontoxic elemental composition. The transport properties for Ca_3AlSb_3 and Zn-doped Ca_3AlSb_3 were experimentally investigated[4, 10], and the thermoelectric properties of Ca_3AlSb_3 were improved via p-type doping to obtain a maximum $ZT = 0.8$ at 1050 K[10]. Sr_3AlSb_3 exhibits a maximum ZT value of 0.1 at 1000 K. Zinc doping has little effect on the carrier concentration in Sr_3AlSb_3 and does not improve the ZT. [7] Comparing the properties for Ca_3AlSb_3 and Sr_3AlSb_3[4, 7, 10] reveals an interesting phenomenon: Zn-doped Sr_3AlSb_3 exhibits a lower carrier concentration than Zn-doped Ca_3AlSb_3 with a maximum ZT value of approximately 0.15 at 800 K[7]. Such a low carrier concentration could cause the low ZT for Sr_3AlSb_3. Hence, improving the low Sr_3AlSb_3 carrier concentration is important to improve its thermoelectric performance. Carrier concentrations always exhibit opposing effects on S, σ, and κ_e. Thus, optimizing the carrier concentration can increase the ZT values for Ca_3AlSb_3 and Sr_3AlSb_3. To explain these phenomenon and improve the thermoelectric properties, we calculated the electronic structures and thermoelectric properties for A_3AlSb_3 (A = Ca, Sr) using a first-principles method and

the semiclassical Boltzmann theory. We found that p-type Ca_3AlSb_3 is a promising thermoelectric compounds along the chain direction. Meanwhile, n-type and p-type Sr_3AlSb_3 may also have good thermoelectric properties via heavy doping.

II. COMPUTATIONAL DETAIL

Experimental A_3AlSb_3 (A = Ca, Sr) structures are used as the initial bulk model and relaxed to obtain the minimum energy structure[11, 12]. The structure was optimized using the projector-augmented-wave (PAW) method based on density functional theory (DFT) as implemented in Vienna *ab initio* simulation package (VASP) [13–15]. The exchange-correlation function was treated with the Perdew-Burke-Ernzerhof (PBE) generalized-gradient approximation (GGA)[16–18]. A plane wave cutoff energy of 500 eV was used throughout. For the Brillouin zone integration, $4 \times 11 \times 3$ and $2 \times 7 \times 4$ Monkhorst-Pack special k-point grids were used for Ca_3AlSb_3 and Sr_3AlSb_3, respectively.

We calculated the electronic structure via the full-potential linearized augmented plane waves (FLAPW) method[19] implemented in WIEN2k [20–22]. The exchange-correlation potential was below the generalized gradient approximation (GGA) as parameterized by Perdew, Burke, and Ernzerhof (PBE)[16]. A plane wave basis cutoff of $R_{mt}K_{max} = 8$ was used. The Muffin tin radius was 2.5 a.u. for Ca, Sr, Al, and Sb. Self-consistent calculations were performed using 500 k points in the irreducible Brillouin zone for both Ca_3AlSb_3 and Sr_3AlSb_3. We obtained accurate band gaps using the modified Becke-Johnson (TB-mBJ)[23] semilocal exchange potential, and the TB-mBJ method reliably predicted the band gap for sp-bonded semiconductors [24]. We included the scalar-relativistic and spin-orbit coupling effects (RSO) to account for Sr due to its large atomic mass.

The thermoelectric properties were evaluated via the semiclassical Boltzmann theory[25–27] as implemented in the Boltz-Trap code[28]. The constant scattering time approximation was used, assuming that the scattering time determining the electrical conductivity does not vary significantly with energy on the scale of kT.

III. RESULTS AND DISCUSSIONS

A. Crystal structure and properties

Two structure types were formed in the A_3AlSb_3 compounds (A = alkaline earth metals): Ca_3InP_3 (No. 62 *Pnma*) and Ba_3AlSb_3 (No. 64 *Cmca*). The tetrahedral A_3AlSb_3 (A = Ca, Sr) structures determined by our simulations are shown in Fig. 1. The figure does not show the A site atoms to better show the tetrahedral $AlSb_4$ arrangement. The Ca_3AlSb_3 had an anisotropic one-dimensional structure that formed a Ca_3InP_3 structure from infinite chains of corner-sharing tetrahedral $AlSb_4$ linked by Ca ions[29]. Sr_3AlSb_3 formed a Ba_3AlSb_3 structure type. The $Al_2Sb_6^{12-}$ dimer in Sr_3AlSb_3 are shown in Fig. 1 and formed from two tetrahedral sharing a common edge as for Al_2Cl_6. Meanwhile, Sr and Sb formed a distorted NaCl-type arrangement with Al in tetrahedral holes.

The optimized structure parameters and bond lengths are listed in Table I and Table II. The lattice constants and atomic positions of the optimized structures are close to the experimental values [11, 12]. The bond lengths between Al and the neighboring Sb atoms in A_3AlSb_3 (A = Ca, Sr) were 2.73 Å, and 2.71 Å, respectively. That is, Sr_3AlSb_3 may have stronger Al-Sb interactions than Ca_3AlSb_3. In addition, Table I indicates each Ca_3AlSb_3 primitive cell contained seven inequivalent atoms, and each Sr_3AlSb_3 one contained five inequivalent atoms. However, each Sr_3AlSb_3 primitive cell had 56 atoms in common with Sr_3GaSb_3, while each Ca_3AlSb_3 cell had only 28 atoms in common. This complex structure suggests Sr_3AlSb_3 should have a lower lattice thermal conductivity (approximately 0.55 W/mK at 1000 K) than Ca_3AlSb_3 (approximately 0.60 W/mK at 1000 K). The large cell and complex structure always induce short mean-path-lengths of heat carrying phonons [30].

Previous experimental work by Zevalkink et al. found Zn-doped Sr_3AlSb_3 possessed a lower carrier concentration than Zn-doped Ca_3AlSb_3 [4, 7, 10]. To explain the low carrier concentration in Sr_3AlSb_3, we calculated the formation energies (E_f) for A_3AlSb_3 (A = Ca, Sr) using a Y atom to replace X (X = Ca, Sr, Al, Sb, Si, Ge, or Sn) in the 1 × 4 × 1 and 1 × 2 × 1 supercell. The formation energy was calculated using

$$E_f = E_{doped} - E_{bulk} - E_X + E_Y, \quad (1)$$

where, E_{doped} and E_{bulk} are the total energies for the supercell containing the substitutional dopant Y and the same bulk A_3AlSb_3 supercell, respectively. E_Y and E_X are the doping

and host atom energies in the bulk phase. The calculated formation energies are shown in Table III. First, Zn more easily replaces Al than Sb. Second, Zn more easily dopes in the Al site in Ca_3AlSb_3 than Sr_3AlSb_3, possibly due to the stronger bond between Al and Sb in Sr_3AlSb_3. Therefore, Zn-doped Sr_3AlSb_3 has a lower carrier concentration than Zn-doped Ca_3AlSb_3, as reported in Ref. [4, 7, 10]. Third, the formation energy for doping the A site is lower for K than Na, which was probably due to K exhibiting a stronger activity than Na. Lastly, the A (A = Ca, Sr) site atom is easier to replace in Ca_3AlSb_3 than Sr_3AlSb_3. *n*-type doping for Ca_3AlSb_3 and Sr_3AlSb_3 has never been performed experimentally. It is interesting to explore the possibility of *n*-type doping in these two compounds. Thus, we also calculated the formation energies of Si, Ge, and Sn on Al sites. As shown in Table III, doping of Sn on Al sites is most easily performed in Ca_3AlSb_3, and doping of Ge in Al site is most easily performed in Sr_3AlSb_3 among Si, Ge, and Sn elements. The calculated formation energies shows that doping of Si, Ge, and Sn on Al site are more difficult than that of Zn on Al site.

B. Transport properties

To optimize the carrier concentration and increase the thermoelectric performance for A_3AlSb_3 (A = Ca, Sr), we calculated the A_3AlSb_3 (A = Ca, Sr) transport coefficients for carrier concentrations from 1×10^{18} to 1×10^{22} cm^{-3} using the semiclassical Boltzmann theory without considering the special dopant type. Fig. 2 shows calculated transport coefficient results for *n*-type and *p*-type A_3AlSb_3 (A = Ca, Sr) at 850 K. Fig. 2(a) shows that the Seebeck coefficients increase and then decrease with increasing carrier concentration. This phenomenon for the Seebeck coefficient at high carrier concentrations can be explained using Eq. 2. For degenerate semiconductors, the Seebeck coefficient is given by

$$S = \frac{8\pi^2 k_B^2}{3eh^2} m^*_{\mathrm{DOS}} T \left(\frac{\pi}{3n}\right)^{2/3}, \tag{2}$$

where k_B is the Boltzmann constant, m^*_{DOS} is the density of states effective mass, T is the temperature, and n is the carrier concentration. The Seebeck coefficients for Sr_3AlSb_3 are larger at low doping concentrations than for Ca_3AlSb_3 mainly due to the larger band gap ($S_{max} = E_g/(2eT_{max})$). The Seebeck coefficients for *p*-doped A_3AlSb_3 are slightly larger than when *n*-doped due to the slightly larger density of states effective mass. Fig. 2(b) shows the

electrical conductivities of A_3AlSb_3 (A = Ca, Sr) as a function of carrier concentration. This figure shows that the electrical conductivities increase with increasing carrier concentration regardless the doping type, which is indicative of thermal carrier activation across the band gap and supports the electrical conductivity being proportional to the carrier concentration ($\sigma = ne\eta$). The electrical conductivity for n-type Ca_3AlSb_3 first increased and then decreased. The σ is much larger for Ca_3AlSb_3 than Sr_3AlSb_3 due to its smaller band mass m_b^* and one-dimensional chain structure. The σ of A_3AlSb_3 is larger for n-doping than p-doping mainly due to the smaller band mass at the bottom of conduction bands than that at the top of valence bands. Fig. 2(c) shows the ZT as a function of carrier concentration. We find the ZT of Sr_3AlSb_3 was larger for n-type doping than p-type doping due to the higher electrical conductivity. The maximum ZT for n-type Sr_3AlSb_3 reached 0.76, which corresponds to a carrier concentration of 4.5×10^{20} e cm^{-3} and is almost equal to the maximum experimental ZT for p-type Ca_3AlSb_3 (0.8 at 1050 K).

It is well known that materials with good thermoelectric properties often have a high anisotropy in their crystal structures[31]. We determined the best transport direction for A_3AlSb_3 (A = Ca and Sr) using the calculated anisotropic transport coefficients for p-type and n-type A_3AlSb_3 (A = Ca, Sr) as a function of the carrier concentration from 1×10^{18} to 1×10^{21} cm^{-3} along the x, y, and z directions at 850 K, without considering special dopants as shown in Fig. 3. This figure shows the anisotropy of the thermoelectric properties was stronger for Ca_3AlSb_3 than Sr_3AlSb_3 due to its band mass anisotropy in different directions and one-dimensional chain in Ca_3AlSb_3. For Ca_3AlSb_3, both the Seebeck coefficient and σ/τ were higher along the y direction than the x and z directions. This phenomenon is consistent with a one-dimensional chain feature along the y direction in Ca_3AlSb_3

C. Electronic structure

The basic bonding features are reflected in the calculated density of states (DOS) for A_3AlSb_3 (A = Ca, Sr) for energies ranging from -2 eV to 2 eV, as shown in Fig. 4. The Ca or Sr cations mainly contribute to the A_3AlSb_3 conduction bands, the top valence bands are dominated by the Sb states, and the Al states appear in both the valence and conduction band edges. The valence band maxima (VBM) is dominated by Sb p states, likely due to non-bonding Sb lone-pairs. The conduction band minimum (CBM) is dominated by the s

and d orbitals. As shown in Fig. 4(c) and (h), the Al s states are dominant at the bottom of conduction band. Fig. 4(d) and (i) show the Sb p states contributions exceed the A p states and Al p states. For Ca_3AlSb_3, the Sb p states differ along the x, y, and z directions. In contrast, the Sb p states for Sr_3AlSb_3 were almost identical in the three directions, which indicates a strong hybridization between the Sb p_x, p_y and p_z.

The calculated band structures for A_3AlSb_3 (A = Ca, Sr) are depicted in the high symmetry directions in Fig. 5, and the corresponding special k points are shown in Fig. S1, ESI. The direct band gap is located at the Γ point for both compounds. There are two bands at the band edge for the upper valence bands. For Ca_3AlSb_3, the two bands at Γ and X are degenerate with a large dispersion. However, the two bands for Sr_3AlSb_3 are not strictly degenerate and have a relative small dispersion. Moreover, the two bands at X split in Sr_3AlSb_3. The difference in the band structures for these two compounds arises from their different polyanionic tetrahedral arrangements. For Ca_3AlSb_3, the edge-sharing anionic tetrahedra form one-dimensional chains. However, for Sr_3AlSb_3, the two edge-sharing tetrahedral form isolated Al_2Sb_6 dimers. The one-dimensional covalent chain feature enhance the covalency degree in the chain direction with a small induced band effective mass in Ca_3AlSb_3. Consequently, Ca_3AlSb_3 exhibits a larger band dispersion in the upper valence bands and lower conduction bands than Sr_3AlSb_3. The carrier mobility determined by A. Zevalkink [4, 7] confirmed this prediction.

The carrier effective mass always exhibits opposing effect on the Seebeck coefficient and carrier mobility. A heavy density-of-states effective mass (m^*_{DOS}) yields a high Seebeck coefficient, and a high mobility always requires a light inertial effective mass (m^*_I) in the transport direction. The m^*_{DOS}, which is determined by the band mass and band degeneracy (N_v), can be defined as

$$m^*_{\mathrm{DOS}} = (m^*_x m^*_y m^*_z)^{1/3} N_v^{2/3}, \tag{3}$$

where m^*_x, m^*_y, and m^*_z are the band mass components along the three perpendicular directions x, y, and z, respectively. Fig. 5 and Table IV show that A_3AlSb_3 band gaps are 0.71 eV and 0.89 eV, which are close to the experimental values of 0.65 eV and 0.70 eV, respectively. The $m^*_{\Gamma-X}$, $m^*_{\Gamma-Y}$, and $m^*_{\Gamma-Z}$ for the p-type Ca_3AlSb_3 are lower than for the p-type Sr_3AlSb_3, which corresponds to the higher carrier mobility in the p-type Ca_3AlSb_3. However, the m^*_{DOS} for the p-type Ca_3AlSb_3 were almost equal to those for p-type Sr_3AlSb_3 due to the double band degeneracy ($N_v = 2$) at the valence band edge for Ca_3AlSb_3. These

results are consistent with the experimental Seebeck coefficient being slightly smaller for p-type Ca_3AlSb_3 than p-type Sr_3AlSb_3. For thermoelectric materials with carriers scattered mainly by acoustic phonons, a light band mass induces a high carrier mobility and improves the thermoelectric performance, which exceeds the detrimental effects on Seebeck coefficient due to the low effective mass [33]. Thus, Ca_3AlSb_3 is a promising thermoelectric material.

The optimal electronic performance for a thermoelectric semiconductor depends on its weighted mobility[2, 34, 35], $\mu(m^*_{\mathrm{DOS}}/m_e)^{\frac{3}{2}}$, where μ and m_e are the carrier mobility and electron mass, respectively. Charge carriers predominantly scattered by acoustic phonons (as occurs in most good thermoelectric materials) are expected to have $\mu \propto 1/m_b^{*\frac{5}{2}}$. Therefore, increasing the band mass should decrease the mobility. However, multiply degenerate valleys produce large m^*_{DOS} without explicitly reducing μ. A large valley degeneracy of N_v can increase m^*_{DOS} to yield a large Seebeck coefficient. Thus, a large valley degeneracy is helpful for thermoelectric materials[36, 37]. A thermoelectric material with a large N_v may simultaneously have light bands (small m_i) and large m^*_{DOS}. The N_v for Ca_3AlSb_3 and Sr_3AlSb_3 are 2 and 1, respectively. The contribution from other bands in heavily doped Sr_3AlSb_3 with maxima at approximately -0.1 eV could potentially lead to an N_v of 2, which corresponds to a carrier concentration of 1×10^{20} cm^{-3}. Thus, a heavily p-type doped Sr_3AlSb_3 may exhibit better thermoelectric properties at carrier concentrations above 1×10^{20} cm^{-3}

IV. CONCLUSION

In summary, the structural, thermoelectric, and electronic properties for A_3AlSb_3 (A = Ca, Sr) were studied using the first-principles calculations and semiclassical Boltzmann theory. We found the different thermoelectric properties for Ca_3AlSb_3 and Sr_3AlSb_3 were mainly derived from their different $AlSb_4$ tetrahedral arrangement. The one-dimensional $AlSb_4$ chain in Ca_3AlSb_3 yields a stronger anisotropy in the thermoelectric properties than for Sr_3AlSb_3 with isolated Al_3Sb_6 dimers. On the one hand, the one-dimensional chain structure for Ca_3AlSb_3 exhibited high electrical conductivities along the chain direction. On the other hand, the double band degeneracy at the valence band edge creates a large Seebeck coefficient for p-type Ca_3AlSb_3. Consequently, Ca_3AlSb_3 may exhibit good thermoelectric properties along the chain direction, which requires further research experiment.

The formation energies calculated for Zn doped at Al sites revealed the origin of lower carrier concentrations of Zn-doped Sr_3AlSb_3 than Zn-doped Ca_3AlSb_3 as reported by experimental workers. The transport properties for Sr_3AlSb_3 indicate the highest achievable ZT for n-type Sr_3AlSb_3 was 0.76, which corresponds to a carrier concentration of 4.5×10^{20} cm^{-3}.

V. ACKNOWLEDGMENTS

This research was sponsored by the National Natural Science Foundation of China (Nos. 51371076 and U1204112), the Program for Innovative Research Team (in Science and Technology) in University of Henan Province (No. 13IRTSTHN017).

[1] G. J. Snyder and E. S. Toberer, Nature Mater. **7**, 105 (2008).

[2] G. A. Slack, CRC Handbook of Thermoelectrics (Ed.: D. M. Rowe), CRC, Boca Raton, FL, p. 406-440 (1995).

[3] Y. L. Yan and Y. X. Wang, J. Mater. Chem. **21**, 12497-12502 (2011).

[4] A. Zevalkink, E. S. Toberer, W. G. Zeier, E. Flaage-Larsen, and G. J. Snyder, Energy Environ. Sci. **4**, 510. (2011).

[5] S. M. Kauzlarich, S. R. Brown, and G. J. Snyder, Dalton Trans. **21**, 2099 (2007).

[6] E. S. Toberer, Andrew F. May, and G. J. Snyder, Chem. Mater. **22**, 624 (2010).

[7] A. Zevalkink, G. Pomrehn, Y. Takagiwa, J. Swallow, and G. J. Snyder, ChemSusChem. **6**, 2316 (2013).

[8] Q. F. Shi, Y. L. Yan, and Y. X. Wang, Appl. Phys. Lett. **104**, 012104 (2014).

[9] L. E. Bell, Science **321**,1457 (2008).

[10] W. G. Zeier, A. Zevalkink, and G. J. Snyder, J. Mater. Chem. **22**, 624 (2010).

[11] G. Cordier, M. Stelter, and H. J. Schaefer, Less-Common Met. **98**, 285 (1984).

[12] G. Cordier, G. Savelsberg, and H. Z. Schaefer, Narurforsch. B **37**, 975 (1982).

[13] G. Kresse and J. Hafner, Phys. Rev. B **47**, 558 (1993).

[14] G. Dresse and J. Hafner, J. Phys.: Condens. Matter **6**, 8245 (1994).

[15] G. Kresse and J. Furthmüller, Phys. Rev. B **54**, 11169 (1996).

[16] J. P. Perdew, K. Burke, and M. Ernzerhof, Phys. Rev. Lett. **77**, 3865 (1996).

[17] P. E. Blöchl, Phys. Rev. B **50**, 17953 (1994).

[18] G. Kresse and D. Joubert, Phys. Rev. B **59**, 1758 (1999).

[19] D. Singh, Planewaves, Pseudopentials, and the LAPW Method, Kluwer Academic, Boston (1994).

[20] D. D. Koelling and B. N. Harmon, J. Phys. C: Solid Phys. **10**, 3107 (1977).

[21] P. Hohenberg and W. Kohn, Phys. Rev. **136**, 864 (1964).

[22] P. Blaha, K. Schwarz, G. K. H. Madsen, D. Kvasnicka, and J. Luitz, WIEN2K, An Augmented Plane Wave+Local Orbitals Program for Calculating Crystal Properties, Vienna University of Technology, Vienna, Austria (2001).

[23] F. Tran and P. Blaha, Phys. Rev. Lett. **102**, 226401 (2009).

[24] D. Koller, F. Tran, and P. Blaha, Phys. Rev. B **83**, 195134 (2011).

[25] J, M. Ziman, Electrons and Phonons, Oxford University Press, New York (2001).

[26] W. Jone and N. H. March, Theoretical Solid State Physics, Courier Dover, New York (1985).

[27] G. K. H. Madsen, K. Schwarz, P. Blaha, and D. J. Singh, Phys. Rev. B **68**, 125212 (2003).

[28] T. Thonhauser, T. J. Scheidemantel, J. O. Sofo, J. V. Badding, and G. D. Mahan, Phys. Rev. B **68**, 085201 (2003).

[29] G. Cordier, H. Schaefer, and M. Stelter, Z. Naturforschung **37b**, 975 (1984).

[30] J. R. Sootsman, D. Y. Chung, and M. G. Kanatzidis, Angew. Chem. Int. Ed. **48**, 8616 (2009).

[31] T. J. Scheidemantel, C. Ambrosch-Draxl, T. Thonhauser, J. V. Badding, and J. O. Sofo, Phys. Rev. B **68** 125210 (2003).

[32] A. D. Becke and K. E. Edgecombe, J. Chem. Phys. **92**, 5397 (1990).

[33] Y. Pei, A. D. Lalonde, H. Wang, and G. J. Snyder, Energy Environ. Sci. **5**, 7963 (2012).

[34] G. D. Mahan, Solid State Physics Vol. 51, Academic Press Inc, San Diego p. 81 (1998).

[35] H. J. Goldsmid, Thermoelectric Refrigeration (Plenum, 1964).

[36] F. J. DiSalvo, Science **285**, 703 (1999).

[37] Y. Pei, X. Shi, A. LaLonde, H. Wang, L. Chen, and G. J. Snyder, Nature **473**, 66 (2011).

TABLE I: Calculated lattice parameters and fractional atomic coordinated for Wyckoff sites of optimized A_3AlSb_3 (A = Ca, Sr)

Lattice parameter	Atomic type	Wyckoff Symbol	x	y	z
Orthorhombic	Ca_1	4c	0.27240	0.25000	0.27952
No. 62 *Pnma*	Ca_2	4c	0.55863	0.25000	0.38798
a=12.9637Å	Ca_3	4c	0.35002	0.25000	0.99673
b=4.5191Å	Al	4c	0.56762	0.25000	0.79666
c=14.3421Å	Sb_1	4c	0.61368	0.25000	0.60928
	Sb_2	4c	0.75644	0.25000	0.88129
	Sb_3	4c	0.04036	0.25000	0.35077
Orthorhombic	Sr_1	8f	0.17600	0.30314	0.12913
No. 64 *Cmca*	Sr_2	16g	0.00000	0.19028	0.35367
a=20.6293Å	Al	8d	0.08617	0.00000	0.00000
b=6.9666Å	Sb_1	8f	0.33948	0.28833	0.12283
c=13.6355Å	Sb_2	16g	0.00000	0.21262	0.10750

FIGURE CAPTIONS

Fig. 1. The tetrahedral structure of A_3AlSb_3 (A = Ca, Sr) with space group *Pnma*, and *Cmca*, respectively. The blue and brown spheres represent Al and Sb atoms, respectively.

Fig. 2. Calculated transport properties of A_3AlSb_3 (A = Ca, Sr): (a) Seebeck coefficients; (b) electrical conductivities; (c) Z_eT.

Fig. 3. Calculated anisotropy of thermoelectric properties of Ca_3AlSb_3 (left) and Sr_3AlSb_3 (right) as a function of carrier concentration from 1×10^{18} to 1×10^{21} cm^{-3} along the x, y, and z directions at 850 K.

Fig. 4. Calculated total and partial DOS for A_3AlSb_3 (A = Ca, Sr). The Fermi level is at zero.

Fig. 5. Calculated band structures of Ca_3AlSb_3 (left panel) and Sr_3AlSb_s (right panel). The high symmetry k points Γ, X, Y, Z, S, U, and R represent the points (0, 0, 0), (0.5,

TABLE II: Calculated bond distances (in Å) of optimized A_3AlSb_3 (A = Ca, Sr)

Atomic type	Nearest neighbor table					
Ca_1	Sb_1 3.14	Sb_3 3.18	Sb_2 3.25	Al 3.26		
Ca_2	Sb_1 3.18	Sb_1 3.25	Sb_2 3.30			
Ca_3	Sb_2 3.17	Sb_3 3.30	Sb_3 3.39	Sb_1 3.42		
Al	Sb_2 2.73	Sb_1 2.75	Sb_3 2.77	Ca_1 3.26		
Sb_1	Al 2.75	Ca_1 3.14	Ca_2 3.18	Ca_2 3.25		
Sb_2	Al 2.73	Ca_3 3.17	Ca_1 3.25	Ca_2 3.30		
Sb_3	Al 2.77	Ca_1 3.18	Ca_3 3.30	Ca_3 3.39		
Sr_1	Al 3.32	Sb_1 3.38	Sb_1 3.40	Sb_1 3.51	Sb_1 3.60	Sb_2 3.70
Sr_2	Sb_2 3.36	Sb_2 3.37	Sb_1 3.40	Sb_1 3.40	Al 3.43	Al 3.43
Al	Sb_1 2.71	Sb_1 2.71	Sb_2 2.74	Sb_2 2.74	Sr_1 3.32	Sr_1 3.72
Sb_1	Al 2.71	Sr_1 3.38	Sr_1 3.40	Sr_2 3.40	Sr_1 3.40	
Sb_2	Al 2.74	Al 2.74	Sr_2 3.36	Sr_2 3.37		

TABLE III: Calculated formation energies (in eV) of A_3AlSb_3 (A = Ca, Sr) by using Y atoms to replace X atoms.

	X = A, Y = Na	X = A, Y = K	X = Al, Y = Zn	X = Sb, Y = Zn
Ca_3AlSb_3	1.23	0.77	0.06	2.1
Sr_3AlSb_3	1.67	1.63	0.24	2.3
	X = Al, Y = Si	X = Al, Y = Ge	X = Al, Y = Sn	
Ca_3AlSb_3	1.13	0.79	0.68	
Sr_3AlSb_3	1.05	0.8	0.9	

0, 0), (0, 0.5, 0), (0, 0, 0.5), (0, 0.5, 0.5), (0.5, 0.5, 0), and (0.5, 0.5, 0.5), respectively.

TABLE IV: Calculated electronic properties of A_3AlSb_3: Band gap (E_g in eV); Band degeneracy (N_v); The band mass along three perpendicular directions (m^* in m_e); and Density of states effective mass ($m^*_{\rm DOS}$ in m_e)

	E_g(eV)	N_v	$m^*_{\Gamma-X}$	$m^*_{\Gamma-Y}$	$m^*_{\Gamma-Z}$	$m^*_{\rm DOS}$
n-type Ca_3AlSb_3	0.71	1	0.67	0.12	0.91	0.42
p-type Ca_3AlSb_3	0.71	2	0.67	0.57	0.62	0.98
n-type Sr_3AlSb_3	0.85	1	0.51	0.36	0.78	0.52
p-type Sr_3AlSb_3	0.85	1	0.87	0.85	1.31	0.99

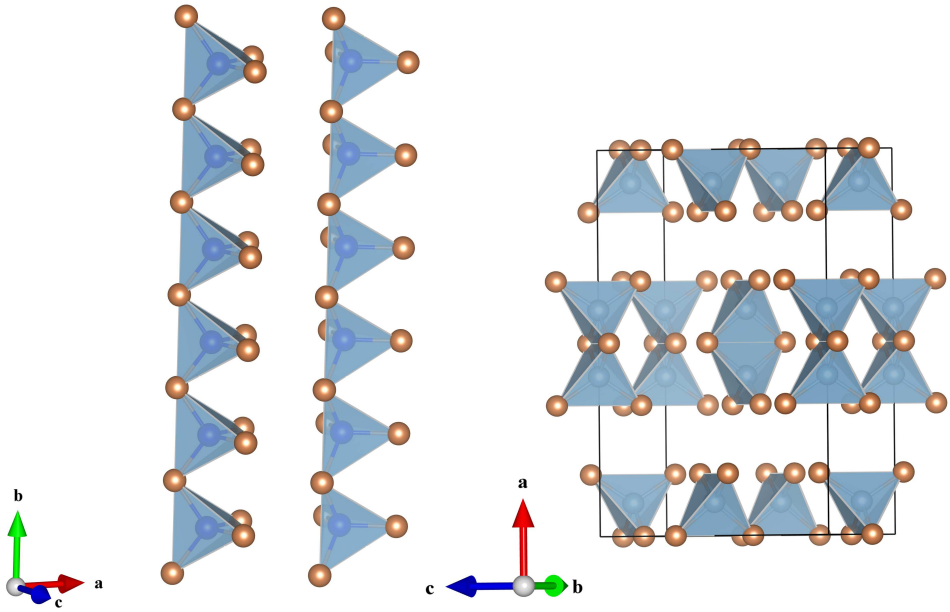

FIG. 1: (Color online) The tetrahedral structure of A_3AlSb_3 (A = Ca, Sr) with space group *Pnma*, and *Cmca*, respectively. The blue and brown spheres represent Al and Sb atoms, respectively.

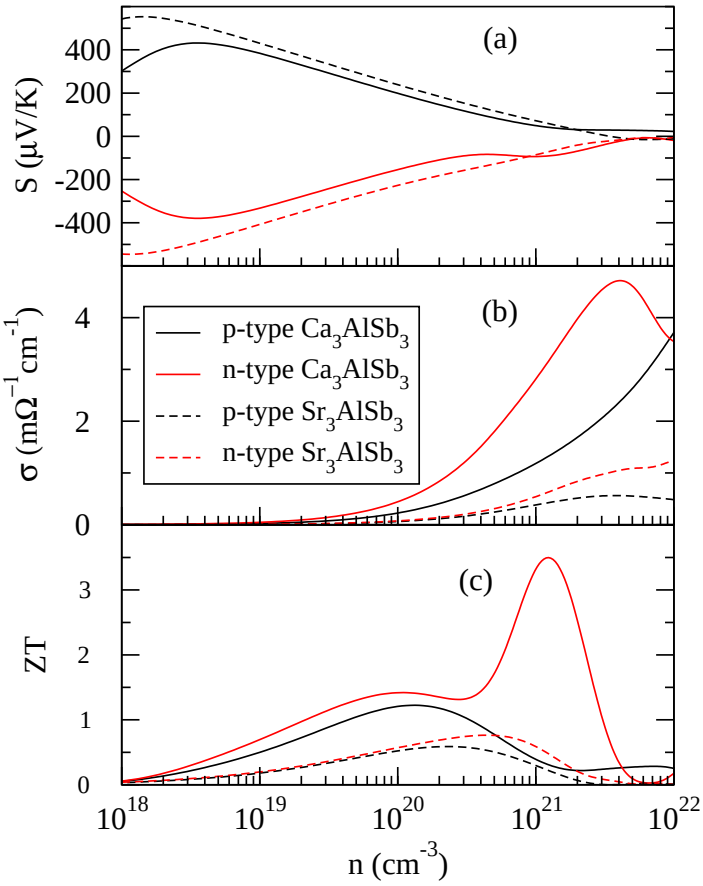

FIG. 2: (Color online) Calculated transport properties of A_3AlSb_3 (A = Ca, Sr): (a) Seebeck coefficients; (b) electrical conductivities; (c) Z_eT.

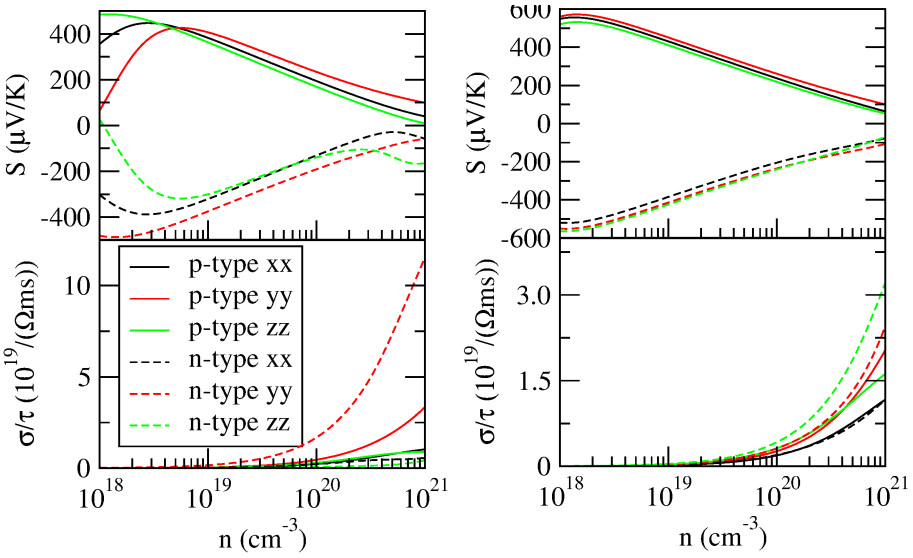

FIG. 3: (Color online) Calculated anisotropy of thermoelectric properties of Ca_3AlSb_3 (left) and Sr_3AlSb_3 (right) as a function of carrier concentration from 1×10^{18} to 1×10^{21} cm^{-3} along the x, y, and z directions at 850 K.

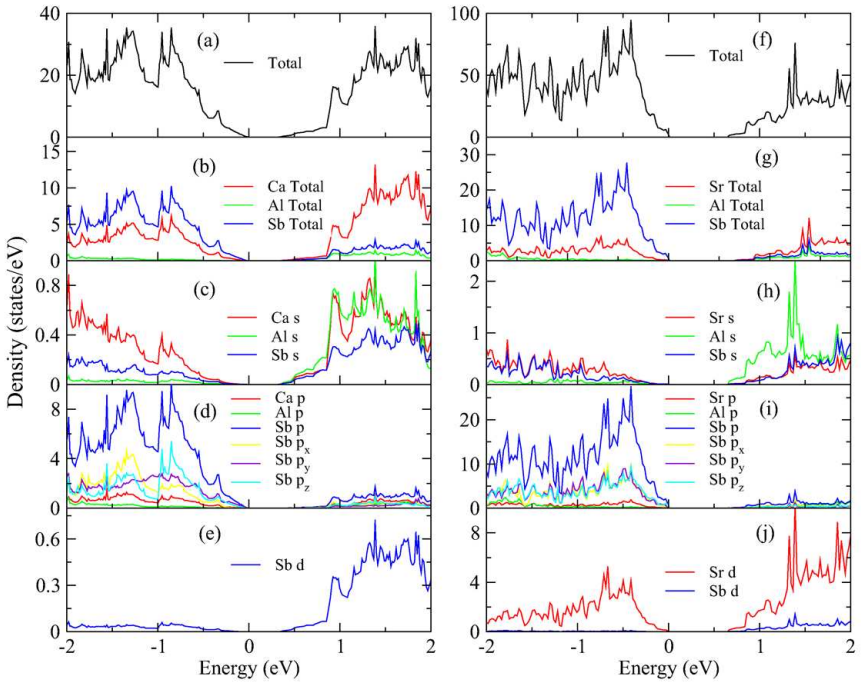

FIG. 4: (Color online) Calculated total and partial DOS for A_3AlSb_3 (A = Ca, Sr). The Fermi level is at zero.

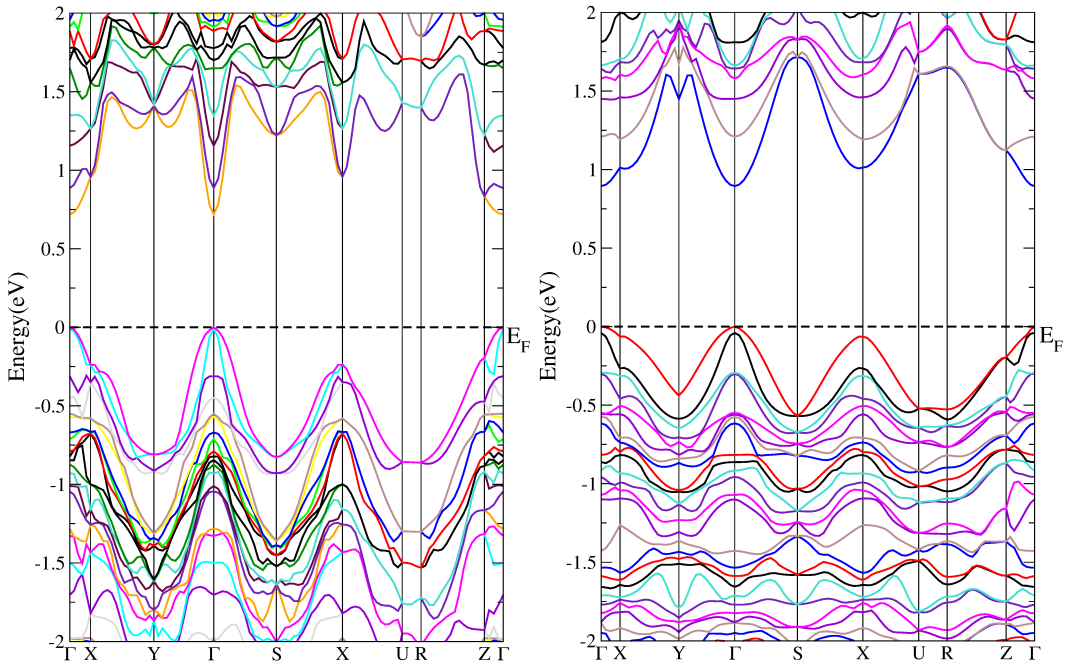

FIG. 5: (Color online) Calculated band structures of Ca_3AlSb_3 (left panel) and Sr_3AlSb_s (right panel). The high symmetry k points Γ, X, Y, Z, S, U, and R represent the points (0, 0, 0), (0.5, 0, 0), (0, 0.5, 0), (0, 0, 0.5), (0, 0.5, 0.5), (0.5, 0.5, 0), and (0.5, 0.5, 0.5), respectively.